Viscoelastic Extracellular Matrix Enhances Epigenetic Remodeling and Cellular Plasticity

Yifan Wu[1], Yang Song[1,9], Jennifer Soto[1], Tyler Hoffman[1], Aaron Zhang[1], Xiao Han[1], Zhiwei Fang[2], Joon Eoh[2], Luo Gu[2], Zhen Gu[1,3,4,5], Song Li[1,6,7,8*]

[1]Department of Bioengineering, University of California, Los Angeles, CA 90095, USA

[2]Department of Materials Science and Engineering and Institute for NanoBioTechnology, Johns Hopkins University, Baltimore, MD 21218, USA

[3]National Key Laboratory of Advanced Drug Delivery and Release Systems, College of Pharmaceutical Sciences, Zhejiang University, Hangzhou 310058, China

[4]Key Laboratory of Advanced Drug Delivery Systems of Zhejiang Province, College of Pharmaceutical Sciences, Zhejiang University, Hangzhou 310058, China

[5]MOE Key Laboratory of Macromolecular Synthesis and Functionalization, Department of Polymer Science and Engineering, Zhejiang University, Hangzhou 310027, China

[6]Department of Medicine, University of California Los Angeles, Los Angeles, CA 90095, USA

[7]Eli and Edythe Broad Center of Regenerative Medicine and Stem Cell Research, University of California Los Angeles, Los Angeles, CA 90095, USA

[8]Jonsson Comprehensive Cancer Center, David Geffen School of Medicine, University of California Los Angeles, Los Angeles, CA 90095, USA

[9]Institute of Biomedical Engineering, West China School of Basic Medical Sciences & Forensic Medicine, Sichuan University, Chengdu 610041, China

*Correspondence: Song Li, Ph.D. Email: songli@ucla.edu

Abstract

Living tissue and extracellular matrices possess viscoelastic properties, but understanding how viscoelastic matrix regulates chromatin and the epigenome is limited. Here, we find that the regulation of the epigenetic state by the viscoelastic matrix is more pronounced on softer matrices. Cells on viscoelastic matrices exhibit larger nuclei, increased nuclear lamina ruffling, loosely organized chromatin, and faster chromatin dynamics, compared to those on elastic matrices. These changes are accompanied by a global increase in euchromatic marks and a local increase in chromatin accessibility at the *cis*-regulatory elements associated with neuronal and pluripotent genes. Consequently, viscoelastic matrices enhanced the efficiency of reprogramming fibroblasts into neurons and induced pluripotent stem cells, respectively. Together, our findings demonstrate the key roles of matrix viscoelasticity in the regulation of epigenetic state, and uncover a new mechanism of biophysical regulation of chromatin and cell reprogramming, with implications for the design of smart materials to engineer cell fate.

Keywords: matrix viscoelasticity, epigenetic state, chromatin dynamics, cell reprogramming

Main

Native tissue and the extracellular matrix (ECM) are biomolecular assemblies possessing viscoelastic properties[1]. With the development of biomaterials with tunable mechanical properties[2-4], viscoelastic effects have been shown to regulate both cell-level processes such as spreading, migration, and differentiation[5-7], and tissue-level behaviors such as matrix formation, morphogenesis, and organoid development[8-11], which underscores the important roles of matrix viscoelasticity in development, disease progression, and tissue regeneration. Although several studies have investigated the cytoskeletal reorganization on viscoelastic surfaces to connect extracellular mechanical changes with intracellular signaling, how matrix viscoelasticity regulates chromatin and the epigenome in the cell nucleus is not well understood.

Accumulative evidence has shown that mechanical stimuli such as compression and matrix stiffness regulate chromatin organization and epigenome to influence the on-off state of lineage-specific genes and thus cell fates[12-17]. To understand how matrix viscoelasticity impacts chromatin structure and activity, we engineered the stiffness and viscoelasticity of matrices, and investigated the genome-wide biophysical and biochemical changes globally and at specific sites. Our findings provide a mechanistic interpretation of the role of viscoelasticity in regulating the cell nucleus, chromatin, and epigenome to modulate cellular plasticity, potentially contributing to the development of smart materials and a new technology platform to engineer cell fate for tissue regeneration, disease modeling, and drug screening.

Stiffness-dependent viscoelastic effects on the cell nucleus and nuclear lamina

Alginate-based hydrogels allow users to tailor viscoelasticity independent of stiffness, pore size, and ligand density[18-20]. We fabricated two groups of alginate gels with varying stiffness and viscoelasticity as described previously[21]. Specifically, 2, 10, and 20 kPa were selected to cover the stiffness range of ECMs in most soft tissue in physiological scenarios[22]. Elastic and viscoelastic gel matrices were fabricated by varying the concentrations of covalent or ionic crosslinkers, respectively (**Fig. 1a**). Rheology measurements showed that gels formed by covalent crosslinking had constant elastic modulus under different frequencies and near-zero loss modulus (**Fig. 1b** and **Extended Data Fig. 1a**). Conversely, the ionic crosslinking afforded gels frequency-dependent elastic moduli and higher loss moduli (**Fig. 1b** and **Extended Data Fig. 1a**), representing their viscoelastic properties. Results from compression tests demonstrated that ionically crosslinked gel matrices displayed faster stress-relaxation under deformation (**Fig. 1c** and **Extended Data Fig. 1b**). Moreover, we confirmed that viscoelastic properties of the gels are independent of stiffness, as the time under constant deformation to relax the initial stress to half of the original value ($\tau_{1/2}$) was similar across different stiffness (~ 670 seconds, **Extended Data Fig. 1c**).

To systemically investigate the influence of matrix viscoelasticity on the cell nucleus, we first sought to examine the nuclear volume based on DAPI staining. Primary fibroblasts isolated from adult mice were seeded on the aforementioned hydrogels made from RGD (Arg-Gly-Asp)-coupled alginate polymers with covalent or ionic crosslinking, where RGD peptides served as ligands for cell adhesion and spreading[18]. While nuclear volume increased with stiffness, cells on viscoelastic matrices displayed larger nuclear volumes when compared to elastic surfaces with the same stiffness, except on 20-kPa surfaces (**Fig. 1d**). Interestingly, cells on viscoelastic gels of 2 kPa exhibited comparable nuclear volume to those on elastic gels of 20 kPa, which was also evident when analyzing cell spreading on different matrices (**Fig. 1d and Extended Data Fig. 2a-b**).

These findings suggest that the viscoelastic effects on the cell nucleus are stiffness-dependent, where cells on soft surfaces show more changes in response to matrix viscoelasticity, in contrast to those on stiffer surfaces.

Further, to assess the structural changes of the nuclear lamina induced by matrix viscoelasticity, mouse fibroblasts were first immunostained for lamin A/C and lamin B1 after culturing on various matrices for 48 hours. While we did not observe a difference in lamin B1 (**Extended Data Fig. 3a**), we found more pronounced nuclear wrinkling on 2-kPa viscoelastic surfaces compared to 2-kPa elastic surfaces, as shown by the lamin A/C staining, and such phenomenon did not occur in cells on stiffer surfaces (10 and 20 kPa) (**Fig. 1e-f**). These findings suggest that a viscoelastic matrix may increase the dynamic remodeling of the nuclear lamina.

Matrix viscoelasticity regulates chromatin condensation and dynamics

As the nuclear lamina bridges chromatin to the cytoskeleton which allows the cell nucleus to sense the mechanical changes in the extracellular environment[23], we postulated that the viscoelastic effects on the nuclear lamina might affect chromatin association. To prove this, we used an ^{m6}A-Tracer GFP reporter that co-expressed with Dam-lamin B1 to label lamina-associated domains (LADs) in chromatin and performed immunofluorescence staining of lamin B1 to identify the association of LAD and nuclear lamina, since the distribution and expression of lamin B1 at the nuclear periphery were comparable in cells on elastic and viscoelastic matrices (**Extended Data Fig. 3a**). We observed that LADs exhibited less co-localization with lamin B1 after a 48-hour culturing of cells on soft viscoelastic matrices, while cells on soft elastic matrices had uninterrupted GFP signals at the nuclear periphery (**Fig. 2a-b**). For stiffer surfaces, there was no obvious structural difference for the LADs (**Fig. 2a-b**). These results indicate that a partial detachment of LADs from the nuclear lamina occurred in cells on soft viscoelastic matrices, which may reorganize the chromatin.

To explore the viscoelastic effects on chromatin organization, we investigated whether viscoelastic matrix regulated the condensation of chromatin as previously described [24,25]. We found that the chromatin compaction index, defined as the ratio of integrated DAPI fluorescence intensity to nuclear volume, decreased with stiffness, and cells on soft viscoelastic surfaces (2 and 10 kPa) had lower chromatin compaction indices, reflecting less chromatin condensation in the cell nucleus (**Fig. 2c-d**). Interestingly, there was no significant change in chromatin compaction on stiffer surfaces (20 kPa) (**Fig. 2c**).

Since the chromatin appeared to be relatively loosely organized in the cell nucleus on soft viscoelastic surfaces, we applied fluorescence recovery after bleaching (FRAP) techniques to directly evaluate the diffusion kinetics of nuclear macromolecules on elastic and viscoelastic matrices. As viscoelastic effects were most pronounced on soft surfaces, we employed 2-kPa hydrogels for all subsequent experiments. After staining the cell nucleus with a live-cell dye (Hoechst 33342), we performed FRAP experiments on loosely packed euchromatic and tightly packed heterochromatic regions indicated by fluorescence-labeled DNA. The results showed that the recovery half time ($t_{1/2}$, the time taken for the bleached region to reach half of its final intensity) was shorter for cells on viscoelastic surfaces in both euchromatic and heterochromatic regions (**Fig. 2e-h**), which suggests that the movement of DNA molecules inside the cell nucleus was faster on viscoelastic surfaces when compared to elastic gels. Moreover, as histones are the major protein

constituents of chromatin besides DNA, we performed similar FRAP experiments utilizing fibroblasts expressing histone H2B with enhanced green fluorescent protein (EGFP) to study histone movement on matrices with different mechanical properties. Consistently, we found that the fluorescence in the bleached regions recovered faster on viscoelastic matrices compared to elastic matrices (**Extended Data Fig. 4a-b**). Collectively, these results indicate that viscoelastic matrices enhance the chromatin reorganization and dynamic chromatin remodeling.

Viscoelastic matrices promote open chromatin marks

As LADs typically reside in a repressive chromatin environment that is enriched with transcriptionally inactive genes[26], the decrease of LAD-lamina association, together with the increase of chromatin dynamics and decrease of chromatin condensation on soft viscoelastic surfaces, suggest an active remodeling of the chromatin. To determine whether these physical changes are accompanied by biochemical modifications of chromatin, we sought to examine the levels of histone marks associated with euchromatin and heterochromatin regions in the cell nucleus. Immunofluorescence analysis results revealed that several euchromatic histone marks, including histone H3 acetylation (AcH3), histone H3 lysine 27 acetylation (H3K27ac), and tri-methylated histone H3 on lysine 4 (H3K4me3), were significantly increased in cells on viscoelastic surfaces (**Fig. 3a-c**), while cells exhibited a slight decrease in tri-methylated histone H3 on lysine 9 (H3K9me3) but not tri-methylated histone H3 on lysine 27 (H3K27me3) that were indicative of heterochromatin (**Extended Data Fig. 5a-b**). The increase of euchromatin marks were further confirmed by the Western blotting assay (**Fig. 3d**).

Next, we analyzed the activities of chromatin-modifying enzymes to investigate their contributions to these epigenetic alterations. Though there was no significant change in histone acetyltransferase (HAT) activity, we found that histone deacetylase (HDAC) activity in cells on viscoelastic surfaces was reduced by half (**Fig. 3e-f**), which could lead to the elevated acetylation level on histone H3. In addition, viscoelastic matrices increased the activity of H3K4- specific histone methyltransferase (HMT) and decreased demethylase (HDM) activity (**Fig. 3g-h**), which could enhance H3K4me3 in cells on viscoelastic surfaces. These findings suggest that viscoelastic matrices regulate histone-modifying enzymes (HDAC, H3K4-specific HMT, and H3K4-specific HDM), which works together to modulate the epigenetic state of cells.

Viscoelastic matrices regulate genome-wide chromatin accessibility and shape cellular plasticity

As matrix viscoelasticity altered chromatin dynamics and the epigenetic state, we hypothesized that elastic and viscoelastic matrices might promote distinct chromatin accessibility landscapes. To examine the genome-wide chromatin accessibility of cells on different surfaces, we performed assay for transposase-accessible chromatin with sequencing (ATAC-seq) on primary mouse fibroblasts to detect permissible chromatin regions associated with different mechanical cues across the genome at the population level.

Principal component analysis (PCA) results of ATAC-seq signals placed elastic groups away from viscoelastic groups along principal component 1 (PC1) that captured 97% of variance, which demonstrated that elastic and viscoelastic surfaces promoted distinct combinations of accessible regions across the genome (**Fig. 4a**). By differential peak analysis, we identified up-regulated and down-regulated peaks in viscoelastic groups compared to elastic groups (**Extended Data Fig. 6a-**

c). We then annotated these differentially expressed peaks to associate them with genomic features including nearest genes and *cis*-regulatory elements such as promoters and enhancers. Compared to the genomic distribution of down-regulated peaks, a higher percentage of the up-regulated peaks was located in promoter regions on viscoelastic surfaces (11.7 %) in comparison to elastic surfaces (6.9 %) (**Fig. 4b**). Since promoters are the initiation point of transcription, the shift in permissible genomic regions in viscoelastic groups suggest that viscoelastic matrices may lower the epigenetic barrier for forced gene expression by external factors.

To further investigate the differences in chromatin accessibility profiles on elastic and viscoelastic matrices, we applied gene ontology (GO) enrichment analysis on genes associated with up- and down-regulated peaks in viscoelastic groups. Results showed that the top 15 enriched GO terms for both up- and down-regulated peaks were not only affiliated with essential biological activities, such as adhesion, migration, and signal transduction, but also related to the development of diverse types of tissue and/or organs coming from mesoderm and ectoderm (**Fig. 4c and Extended Data Fig. 6d-e**). These multi-directional changes in the shift of permissible chromatin regions in cells on viscoelastic surfaces indicated a potential role of matrix viscoelasticity in regulating cellular plasticity. To test whether this may be possible, we first examined chromatin accessibility around lineage-determining transcription factors and lineage-specific marker genes in elastic and viscoelastic groups using publicly available chromatin immunoprecipitation followed by sequencing (ChIP-seq) datasets. By plotting ATAC signals in the shared regions between the recognized peaks in certain ChIP-seq datasets and our differentially expressed peaks, we were able to explore the accessibility changes around the genomic targets of pioneer transcription factors that played important roles in regulating cell fate decisions in development and reprogramming. Analysis of Ascl1 (neuronal lineage)[27], MyoD (myogenic lineage)[28], ETV2 (endothelial and hematopoietic lineage)[29], and Oct4 (pluripotency)[30] target sites demonstrated that matrix viscoelasticity remodeled chromatin organization to increase accessibility around genomic regions actively involved in neuronal and pluripotent lineages in fibroblasts, while regions around hematoendothelial genes exhibited a more closed structure on viscoelastic surfaces (**Fig. 4d**). In addition, the promoters of typical mesenchymal cell markers (*Eng* [CD105] and *Nt5e* [CD73]) and an epithelial-mesenchymal transition regulator (*Prrx1*) displayed lower accessibility in viscoelastic groups compared to elastic groups (**Extended Data Fig. 6f**), which implied that the fibroblasts on viscoelastic matrices might be easier to reprogrammed into neuronal or pluripotent cells.

Viscoelastic matrices promote induced neuronal (iN) reprogramming from mouse fibroblasts

To investigate whether matrix viscoelasticity enhanced cell phenotype transition in response to external factor-driven gene activation due to epigenetic and chromatin permissibility changes, we employed a direct reprogramming model that converted mouse fibroblasts to neurons by lentiviral transduction of three transcription factors (Brn2, Ascl1, Myt1l, abbreviated as BAM)[31]. As there was an increase in chromatin accessibility around Ascl1-targeting genomic sites on viscoelastic surfaces (**Fig. 4d**), we hypothesized that fibroblasts on viscoelastic matrices could be reprogrammed into neurons more efficiently. Indeed, we found that chromatin regions near the promoters of *Brn2*, *Ascl1*, and *Myt1l* were more permissible in viscoelastic groups compared to elastic (**Fig. 5a**). To test the effect of matrix viscoelasticity on induced neuronal (iN) reprogramming, primary mouse fibroblasts were transduced with doxycycline (Dox)-inducible lentiviral vectors encoding BAM and the following day the cells were seeded onto elastic and

viscoelastic matrices. Twenty-four hours later, Dox was added to the culture media to induce the expression of the transgenes and initiate the reprogramming process (marked as day 0). Neuronal medium containing Dox was used for cell culture from day 1 to the conclusion of the experiment (**Fig. 5b**).

To monitor the viscoelastic effects on cell phenotype conversion during the course of reprogramming, we first collected samples on day 2 to examine endogenous *Ascl1* expression in cells on elastic and viscoelastic surfaces, since Ascl1 serves as a pioneer factor in iN reprogramming that immediately binds to its genomic sites after induction and recruits other transcription factors[27]. We observed a ~ 5-fold increase of endogenous *Ascl1* expression in cells collected from viscoelastic matrices compared to those on elastic matrices (**Fig. 5c**). Furthermore, we isolated fibroblasts from TauEGFP knock-in mice that expressed enhanced GFP (EGFP) after the expression of neuron-specific microtubule-associated protein (Tau) and conducted iN reprogramming following the same procedure. On day 5, the percentage of cells expressing Tau-GFP on viscoelastic surfaces was ~ 6-fold higher than those on elastic surfaces (**Fig. 5d**). To determine the reprogramming efficiency of iN conversion, we reprogrammed the cells on the various matrices and on day 7, samples were fixed and immunostained for the neuronal marker, Tubb3 (neuron-specific class III beta-tubulin). We found that viscoelastic matrices led to a significantly higher iN conversion efficiency compared to elastic surfaces (**Fig. 5e-f**), as determined by the percentage of $Tubb3^+$ cells among the total number of seeded cells. Moreover, we cultured iN cells on different surfaces for 3 or 4 weeks for further characterization and found that iN cells expressed mature neuronal markers, microtubule-associated protein 2 (MAP2) and synapsin, on both surfaces after 3 weeks (**Fig. 5g and Extended Data Fig. 7a**). Furthermore, iN cells exhibited calcium fluctuations, indicating that these cells were functional (**Supplementary Video 1**). Based on these findings, we concluded that matrix viscoelasticity boosted the reprogramming of adult mouse fibroblasts into neurons.

To evaluate whether the regulation of matrix viscoelasticity on iN reprogramming was a consequence of the viscoelastic effects on chromatin organization and epigenetic state, we used a small-molecule inhibitor of HDAC (valproic acid, VPA) to disrupt HDAC activity, which can lead to an increase in histone acetylation and thus, contributes to a more open chromatin structure (**Extended Data Fig. 7b-d**). Upon reprogramming fibroblasts on various matrices in the absence or presence of an HDAC inhibitor, we found that HDAC inhibition enhanced the iN reprogramming efficiency of cells on elastic matrices to an extent similar to cells on viscoelastic matrices without inhibitor treatment, but did not further enhance the reprogramming efficiency on viscoelastic surfaces (**Extended Data Fig. 7b and Fig. 5h**), suggesting that the downregulation of HDAC by viscoelastic matrices may play a role in regulating viscoelasticity-mediated cell phenotype conversion. Together, these results demonstrate that matrix viscoelasticity facilitates cell phenotype transition by regulating the chromatin and epigenome in the cell nucleus.

Viscoelastic matrices promote induced pluripotent stem cell (iPSC) reprogramming from mouse fibroblasts

To further validate our hypothesis that matrix viscoelasticity reshaped cellular plasticity by altering the chromatin landscape with increased accessibility in the regions near lineage-specific genes, we investigated the effect of viscoelasticity on iPSC reprogramming given that the chromatin accessibility of Oct4-targeting genomic regions was substantially increased in cells on viscoelastic

surfaces (**Fig. 4d**). For these experiments, primary adult mouse fibroblasts were transduced with Oct4, Sox2, Klf4, and c-MYC (OSKM) transcription factors and cultured on elastic or viscoelastic gels for 10 days (**Fig. 6a**). Interestingly, we observed a ~12-fold enhancement in the percentage of $Nanog^+$ colonies on viscoelastic matrices, where the $Nanog^+$ colonies were also larger in size compared to elastic surfaces (**Fig. 6b-c**). These findings were further supported by PCR analysis results which showed a significant increase in *Nanog* expression from cells cultured on viscoelastic matrices compared to the elastic group (**Fig. 6d**). Moreover, we found that ATAC peaks near the promoter region of *Nanog* had a significantly higher signal in the viscoelastic group compared to elastic (**Fig. 6e**), which is in agreement with our reprogramming and gene expression findings (**Fig. 6b-d**).

Outlook

Here we show, for the first time, that matrix viscoelasticity can regulate the organization and dynamics of chromatin and the epigenome to facilitate changes in cellular plasticity (**Fig. 6f**). Cells on soft matrices are more responsive to external viscoelastic signals, while stiff matrices desensitize cells to matrix viscoelasticity, as illustrated in cell volume, nuclear lamina wrinkling, LAD dissociation, chromatin compaction, and chromatin dynamics. Compared to soft elastic matrices, cells on soft viscoelastic matrices have larger cell nuclei, more nuclear wrinkling, increased LAD dissociation, less compacted chromatin, and faster nuclear molecular diffusions of chromatin within the cell nucleus. The increase of nucleus volume on viscoelastic surfaces (2 kPa) may result from the enhanced cell spreading due to the stress relaxation at cell adhesions[5]. In addition, the enhanced dynamic cellular processes such as cell migration on viscoelastic surfaces[7] may exert dynamic forces on the nucleus, leading to the deformation and lamina wrinkling of nucleus, although this is mild in comparison to transient mechanical squeezing of cells[16]. These mechanical changes in the nuclear lamina may cause LAD dissociation, faster chromatin dynamics and less chromatin compaction. Nonetheless, further evaluation of epigenetic changes shows an increase in open chromatic marks, a decrease of HDAC activity, an increase of H3K4-specific HMT, and a decrease of H3K4-specific HDM activity on viscoelastic surfaces, suggesting that biochemical signaling also mediates and contributes to the regulation of epigenetic states by viscoelastic surfaces.

As reported previously, the disruption of intracellular actomyosin contractility using small-molecule inhibitors caused less cell spreading, but induced nuclear wrinking, an increase of euchromatin marks, a decrease of heterochromatin marks, and enhanced chromatin accessibility at the promoters of neuronal genes were also exhibited in the inhibitor-treated cells[36]. This apparent contradictory observation could be explained by the enhanced chromatin remodeling due to the release of intracellular constraints as well as biochemical signaling to promote a more open chromatin structure.

Interestingly, the chromatin landscapes modulated by viscoelastic surfaces are similar to those in undifferentiated embryonic stem cells (ESCs). ESCs are found to possess little nuclear lamina constraints, decondensed chromatin organization, enhanced chromatin protein dynamics, and enrichment in euchromatic marks, compared to differentiated cells[32-35], which makes them highly plastic and prone to differentiate into various cell types. Our findings suggest that matrix viscoelasticity may shape the cellular plasticity towards the direction similar to multipotent and/or pluripotent cells, which creates a favorable epigenetic state for cell phenotype transitions. These

findings may guide the future development of novel biomaterials with tunable mechanical properties for more effective cell phenotype conversion.

Furthermore, as the alterations in tissue mechanics occurs enormously in development, aging, and disease progression[37-39], our findings of the stiffness-dependent viscoelastic effects on the cell nucleus, chromatin, and the epigenome also have important implications in cellular responses to the changing ECM mechanical properties during aging and disease development. For example, diverse pathological conditions are accompanied with an increase in viscoelasticity and stiffness, such as fibrosis[40] and most malignant tumors[41], while some diseases (e.g., diabetes and obesity) can make the local tissue softer and more viscoelastic. These changes in mechanical environment may have profound effects on the differentiation, de-differentiation and trans-differentiation of tissue-resident cells, which warrants further investigations in disease-specific contexts.

References

1 Chaudhuri, O., Cooper-White, J., Janmey, P. A., Mooney, D. J. & Shenoy, V. B. Effects of extracellular matrix viscoelasticity on cellular behaviour. *Nature* **584**, 535-546, doi:10.1038/s41586-020-2612-2 (2020).

2 Chakma, P. & Konkolewicz, D. Dynamic Covalent Bonds in Polymeric Materials. *Angew. Chem. Int. Ed. Engl.* **58**, 9682-9695, doi:10.1002/anie.201813525 (2019).

3 Rosales, A. M. & Anseth, K. S. The design of reversible hydrogels to capture extracellular matrix dynamics. *Nat. Rev. Mater.* **1**, doi:10.1038/natrevmats.2015.12 (2016).

4 Nguyen, A. K. *et al.* Hierarchical assembly of tryptophan zipper peptides into stress-relaxing bioactive hydrogels. *Nat. Commun.* **14**, 6604, doi:10.1038/s41467-023-41907-1 (2023).

5 Chaudhuri, O. *et al.* Substrate stress relaxation regulates cell spreading. *Nat. Commun.* **6**, 6364, doi:10.1038/ncomms7365 (2015).

6 Chaudhuri, O. *et al.* Hydrogels with tunable stress relaxation regulate stem cell fate and activity. *Nat. Mater.* **15**, 326-334, doi:10.1038/nmat4489 (2016).

7 Adebowale, K. *et al.* Enhanced substrate stress relaxation promotes filopodia-mediated cell migration. *Nat. Mater.* **20**, 1290-1299, doi:10.1038/s41563-021-00981-w (2021).

8 Lee, H. P., Gu, L., Mooney, D. J., Levenston, M. E. & Chaudhuri, O. Mechanical confinement regulates cartilage matrix formation by chondrocytes. *Nat. Mater.* **16**, 1243-1251, doi:10.1038/nmat4993 (2017).

9 Wei, Z., Schnellmann, R., Pruitt, H. C. & Gerecht, S. Hydrogel Network Dynamics Regulate Vascular Morphogenesis. *Cell Stem Cell* **27**, 798-812 e796, doi:10.1016/j.stem.2020.08.005 (2020).

10 Hunt, D. R. *et al.* Engineered Matrices Enable the Culture of Human Patient-Derived Intestinal Organoids. *Adv. Sci. (Weinh)* **8**, 2004705, doi:10.1002/advs.202004705 (2021).

11 Elosegui-Artola, A. *et al.* Matrix viscoelasticity controls spatiotemporal tissue organization. *Nat. Mater.* **22**, 117-127, doi:10.1038/s41563-022-01400-4 (2023).

12 Crowder, S. W., Leonardo, V., Whittaker, T., Papathanasiou, P. & Stevens, M. M. Material Cues as Potent Regulators of Epigenetics and Stem Cell Function. *Cell Stem Cell* **18**, 39-52, doi:10.1016/j.stem.2015.12.012 (2016).

13 Kalukula, Y., Stephens, A. D., Lammerding, J. & Gabriele, S. Mechanics and functional consequences of nuclear deformations. *Nat. Rev. Mol. Cell Biol.* **23**, 583-602, doi:10.1038/s41580-022-00480-z (2022).

14 Huebsch, N. *et al.* Harnessing traction-mediated manipulation of the cell/matrix interface to control stem-cell fate. *Nat. Mater.* **9**, 518-526, doi:10.1038/nmat2732 (2010).
15 Downing, T. L. *et al.* Biophysical regulation of epigenetic state and cell reprogramming. *Nat. Mater.* **12**, 1154-1162, doi:10.1038/nmat3777 (2013).
16 Song, Y. *et al.* Transient nuclear deformation primes epigenetic state and promotes cell reprogramming. *Nat. Mater.* **21**, 1191-1199, doi:10.1038/s41563-022-01312-3 (2022).
17 Song, Y. *et al.* Biphasic regulation of epigenetic state by matrix stiffness during cell reprogramming. *Sci. Adv.* **10**, eadk0639, doi:10.1126/sciadv.adk0639 (2024).
18 Rowley, J. A., Madlambayan, G. & Mooney, D. J. Alginate hydrogels as synthetic extracellular matrix materials. *Biomaterials* **20**, 45-53, doi:Doi 10.1016/S0142-9612(98)00107-0 (1999).
19 Zhao, X., Huebsch, N., Mooney, D. J. & Suo, Z. Stress-relaxation behavior in gels with ionic and covalent crosslinks. *J. Appl. Phys.* **107**, 63509, doi:10.1063/1.3343265 (2010).
20 Tan, X. *et al.* Integrin and syndecan binding peptide-conjugated alginate hydrogel for modulation of nucleus pulposus cell phenotype. *Biomaterials* **277**, 121113, doi:10.1016/j.biomaterials.2021.121113 (2021).
21 Charbonier, F., Indana, D. & Chaudhuri, O. Tuning Viscoelasticity in Alginate Hydrogels for 3D Cell Culture Studies. *Curr. Protoc.* **1**, e124, doi:10.1002/cpz1.124 (2021).
22 Guimarães, C. F., Gasperini, L., Marques, A. P. & Reis, R. L. The stiffness of living tissues and its implications for tissue engineering. *Nat. Rev. Mater.* **5**, 351-370, doi:10.1038/s41578-019-0169-1 (2020).
23 Dupont, S. & Wickstrom, S. A. Mechanical regulation of chromatin and transcription. *Nat. Rev. Genet.* **23**, 624-643, doi:10.1038/s41576-022-00493-6 (2022).
24 Versaevel, M., Grevesse, T. & Gabriele, S. Spatial coordination between cell and nuclear shape within micropatterned endothelial cells. *Nat. Commun.* **3**, 671, doi:10.1038/ncomms1668 (2012).
25 Luciano, M. *et al.* Cell monolayers sense curvature by exploiting active mechanics and nuclear mechanoadaptation. *Nat. Phys.* **17**, 1382-1390, doi:10.1038/s41567-021-01374-1 (2021).
26 Gruenbaum, Y. & Foisner, R. in *Annu. Rev. Biochem.* Vol. 84 *Annual Review of Biochemistry* (ed R. D. Kornberg) 131-164 (2015).
27 Wapinski, O. L. *et al.* Hierarchical mechanisms for direct reprogramming of fibroblasts to neurons. *Cell* **155**, 621-635, doi:10.1016/j.cell.2013.09.028 (2013).
28 Wang, R. *et al.* MyoD is a 3D genome structure organizer for muscle cell identity. *Nat. Commun.* **13**, 205, doi:10.1038/s41467-021-27865-6 (2022).
29 Gong, W. *et al.* ETV2 functions as a pioneer factor to regulate and reprogram the endothelial lineage. *Nat. Cell Biol.* **24**, 672-684, doi:10.1038/s41556-022-00901-3 (2022).
30 Soufi, A. *et al.* Pioneer transcription factors target partial DNA motifs on nucleosomes to initiate reprogramming. *Cell* **161**, 555-568, doi:10.1016/j.cell.2015.03.017 (2015).
31 Vierbuchen, T. *et al.* Direct conversion of fibroblasts to functional neurons by defined factors. *Nature* **463**, 1035-1041, doi:10.1038/nature08797 (2010).
32 Meshorer, E. & Misteli, T. Chromatin in pluripotent embryonic stem cells and differentiation. *Nat. Rev. Mol. Cell Biol.* **7**, 540-546, doi:10.1038/nrm1938 (2006).
33 Constantinescu, D., Gray, H. L., Sammak, P. J., Schatten, G. P. & Csoka, A. B. Lamin A/C expression is a marker of mouse and human embryonic stem cell differentiation. *Stem Cells* **24**, 177-185, doi:10.1634/stemcells.2004-0159 (2006).

34 Melcer, S. *et al.* Histone modifications and lamin A regulate chromatin protein dynamics in early embryonic stem cell differentiation. *Nat. Commun.* **3**, 910, doi:10.1038/ncomms1915 (2012).
35 Pajerowski, J. D., Dahl, K. N., Zhong, F. L., Sammak, P. J. & Discher, D. E. Physical plasticity of the nucleus in stem cell differentiation. *Proc. Natl. Acad. Sci. U. S. A.* **104**, 15619-15624, doi:10.1073/pnas.0702576104 (2007).
36 Soto, J. *et al.* Reduction of Intracellular Tension and Cell Adhesion Promotes Open Chromatin Structure and Enhances Cell Reprogramming. *Adv. Sci. (Weinh)*, e2300152, doi:10.1002/advs.202300152 (2023).
37 Bonnans, C., Chou, J. & Werb, Z. Remodelling the extracellular matrix in development and disease. *Nat. Rev. Mol. Cell Biol.* **15**, 786-801, doi:10.1038/nrm3904 (2014).
38 Phillip, J. M., Aifuwa, I., Walston, J. & Wirtz, D. in *Annu. Rev. Biomed. Eng.* Vol. 17 *Annual Review of Biomedical Engineering* (ed M. L. Yarmush) 113-141 (2015).
39 Mohammadi, H. & Sahai, E. Mechanisms and impact of altered tumour mechanics. *Nat. Cell Biol.* **20**, 766-774, doi:10.1038/s41556-018-0131-2 (2018).
40 Distler, J. H. W. *et al.* Shared and distinct mechanisms of fibrosis. *Nat. Rev. Rheumatol.* **15**, 705-730, doi:10.1038/s41584-019-0322-7 (2019).
41 Rus, G., Faris, I. H., Torres, J., Callejas, A. & Melchor, J. Why Are Viscosity and Nonlinearity Bound to Make an Impact in Clinical Elastographic Diagnosis? *Sensors (Basel)* **20**, doi:10.3390/s20082379 (2020).
42 Martin, M. Cutadapt removes adapter sequences from high-throughput sequencing reads. *EMBnet.journal* **17**, doi:10.14806/ej.17.1.200 (2011).
43 Langmead, B. & Salzberg, S. L. Fast gapped-read alignment with Bowtie 2. *Nat. Methods* **9**, 357-359, doi:10.1038/nmeth.1923 (2012).
44 Danecek, P. *et al.* Twelve years of SAMtools and BCFtools. *Gigascience* **10**, doi:10.1093/gigascience/giab008 (2021).
45 Zhang, Y. *et al.* Model-based analysis of ChIP-Seq (MACS). *Genome Biol.* **9**, R137, doi:10.1186/gb-2008-9-9-r137 (2008).
46 Liao, Y., Smyth, G. K. & Shi, W. featureCounts: an efficient general purpose program for assigning sequence reads to genomic features. *Bioinformatics* **30**, 923-930, doi:10.1093/bioinformatics/btt656 (2014).
47 Love, M. I., Huber, W. & Anders, S. Moderated estimation of fold change and dispersion for RNA-seq data with DESeq2. *Genome Biol.* **15**, 550, doi:10.1186/s13059-014-0550-8 (2014).
48 Wu, T. *et al.* clusterProfiler 4.0: A universal enrichment tool for interpreting omics data. *Innovation (Camb)* **2**, 100141, doi:10.1016/j.xinn.2021.100141 (2021).
49 Robinson, J. T. *et al.* Integrative genomics viewer. *Nat. Biotechnol.* **29**, 24-26, doi:10.1038/nbt.1754 (2011).

Methods

Alginate hydrogel preparation

Sodium alginate (Sigma-Aldrich, PRONOVA UP MVG) with over 60% of its unit as guluronate monomer units and an average molecular weight over 200 kDa was used to prepare elastic and viscoelastic hydrogels[21]. Briefly, sodium alginate was dissolved in MES buffer (0.1 M MES, 0.3 M NaCl, pH 6.5) or Dulbecco's modified Eagle's medium (DMEM) at 2.5% wt/vol to make the alginate solution for elastic or viscoelastic gels. Crosslinker solutions was prepared prior to gel fabrication, where appropriate amounts of adipic acid dihydrazide (AAD, from Sigma) was dissolved in MES buffer containing 2.5 mg ml^{-1} of 1-Hydroxybenzotriazole (HOBt, from Sigma) and 50 mg ml^{-1} N-(3-Dimethylaminopropyl)-N'-ethylcarbodiimide (EDC, from Sigma) as covalent crosslinker solutions and different concentrations of calcium sulfate was evenly distributed into DMEM as ionic crosslinker solutions. 0.8 ml of alginate solution was mixed with 0.2 ml of crosslinker solution using two syringes and deposited between two hydrophobically treated glass slides with a spacer of various heights. Ionically crosslinked hydrogels and covalently crosslinked hydrogels were put into DMEM after 2 or 12 hours of gelation, respectively, and washed two times per day for 2 days to remove unused crosslinkers. For cell-adhesive hydrogels, an oligonucleotide with the sequence of GGGGRGDSP (Genscript) of 100 mg was conjugated to the alginate polymer (1 g) through the reaction with EDC (484 mg) and N-hydroxysulfosuccinimide (sulfo-NHS, 274 mg) in 1% (wt/vol in MES buffer) alginate solution for 20 h. The resulting solution was dialyzed against deionized water for 3 days (molecular weight cutoff of 3.5 kDa), sterile-filtered, and lyophilized before being reconstituted into MES buffer or DMEM to make the hydrogels. The concentrations of AAD solutions to make elastic gels were 1.5, 6, 15 mM and the calcium concentrations in the calcium sulfate crosslinker solutions used to fabricate viscoelastic gels were 45, 90, 150 mM, respectively. The final concentration of alginate in the hydrogels was 2% (wt/vol).

Mechanical characterization of hydrogels

The mechanical properties of covalently and ionically crosslinked hydrogels were determined using rheology measurements and compression tests. To measure the rheological properties, hydrogels were made at the same day of the rheology test. A small-amplitude strain sweep with a constant frequency at 0.5 rad/s was performed to find the linear elastic regime, followed by a frequency sweep at 0.5% strain and a full-amplitude strain sweep at 0.5 rad/s to assess the storage modulus and loss modulus using a rheometer (Anton Paar MCR302). The stiffness and stress relaxation properties were measured from compression tests on alginate gels after one-day equilibrium in DMEM. The gels were compressed to 25% strain with a deformation rate of 1 mm min^{-1} using a Chatillon TCD 225 series Force Measurement System. Afterward, the strain was held constant and the load was recorded over time. The initial stiffness of the hydrogels was calculated using the slope of the stress-strain curve at 5-10% strain. To find $\tau_{1/2}$ (the time that gels took to relax their initial stress to its half value) of different gels, stress-relaxing curves were fitted into a biexponential equation based on a two-element Maxwell-Weichert model and $\tau_{1/2}$ was calculated from each curve.

Fibroblast isolation, culture, and cell seeding

Mice utilized in these studies were housed under specific pathogen-free conditions and 12-hour-light/12-hour-dark cycles with a control of temperature (20-26 °C) and humidity (30-70%). All experiments, including breeding, maintenance and euthanasia of animals, were performed in

accordance with relevant guidelines and ethical regulations approved by the UCLA Institutional Animal Care and Use Committee (protocol no. ARC-2016-036 and ARC-2016-101).

Ear fibroblasts were isolated from adult C57BL/6 mice of 1 month old (male and female, from Jackson Laboratory, 000664), Tau-EGFP reporter mice (Jackson Laboratory, 004779) and R26-M2rtTA;Col1a1-tetO-H2B-GFP compound mutant mice (Jackson Laboratory, 016836). Cells were expanded in mouse embryonic fibroblast (MEF) medium after isolation: DMEM (Gibco) with the addition of 10% fetal bovine serum (FBS, from Gibco) and 1% penicillin/streptomycin (Gibco), and used at passage 2 for all experiments. Fibroblasts were plated on the surface of hydrogels at an initial density of 10,000 cells cm^{-2} to allow for cell-ECM interactions with minimal interference from cell-cell interactions. MEF medium was added to the hydrogels 2 hours after cell seeding to ensure cell attachment. To observe cell spreading and cell nuclear differences on different matrices, cells were cultured on hydrogels for 24 h before being fixed and stained for analysis.

Immunofluorescent staining and quantification

For immunostaining, the gels were fixed with 4% paraformaldehyde (Electron Microscopy Sciences) in serum-free DMEM for 30 min after removing the media and washing with serum-free DMEM once. Gels were then washed three times in serum-free DMEM, permeabilized with 0.5% Triton-X-100 (Sigma), and blocked with 5% donkey serum (Jackson Immunoresearch) in serum-free DMEM following standard immunostaining protocols[36]. For actin-cytoskeleton staining, samples were incubated with Alexa Fluor 635 phalloidin (Invitrogen) for 1 h. Primary antibodies (refer to **Table S1, Supplementary Information**) were incubated overnight at 4 °C, followed by 1-h incubation with Alexa 488 and/or Alexa 546-labeled secondary antibodies (Molecular Probes). Nuclei were stained with 4,6-diamino-2-phenylindole (DAPI) (Invitrogen). Epifluorescence images were collected using a Zeiss Axio Observer Z1 inverted fluorescence microscope, whereas confocal images were acquired using Leica SP8 Confocal Laser Scanning microscope.

Fluorescence intensity-based quantifications were performed using ImageJ macros. To quantify nuclear volume and chromatin compaction index, DAPI-stained nuclei images were taken from the bottom to the top using z-stack function with a step size of 300 nm. For each individual nuclei, the maximum intensity was projected using Image J, followed by Gaussian blur and thresholding to obtain the mask. The mask was then applied to each individual slice of the corresponding nuclei to quantify the area of the nuclei sections. Nuclear volume was calculated as the sum of the area in each slice multiplied by the step size. Chromatin compaction index was determined as the ratio of the integrated fluorescence intensity of the sum intensity of all slices for each individual nuclei to the corresponding nuclear volume as previously described[25]. To calculate the nuclear wrinkling index, the inner part of the cell nucleus was identified using the erode function on the segmented cell nucleus based on DAPI or lamin A/C staining and the average fluorescence intensity of the inner part was measured. To quantify fluorescence intensity of histone staining, DAPI-stained nuclei were segmented using Gaussian blur, thresholding, watershed, and analyze particle functions to identify individual nuclei. The obtained mask was applied to the corresponding stained fluorescence channel to quantify the average fluorescence intensity within each nucleus.

To quantify the reprogramming efficiency from fibroblasts to induced neuronal (iN) cells, gels were fixed and immunostained for Tubb3 (neuron-specific class III beta-tubulin) after 7 days of culturing. iNs were identified based on displays of a typical neuronal morphology (defined as cells with a circular cell body containing a neurite that was at least two times the length of the cell

body) and positive Tubb3 expression as previously described[31]. The reprogramming efficiency was calculated as the percentage of $Tubb3^+$ iN cells from the total cells initially plated. To count iPSC colonies, gels were fixed and immunostained for Nanog after 10 days of culturing. Colonies with positive Nanog expression were identified as iPSC colonies.

^{m6}A Tracer labeling of LADs

To label lamina-associated domains (LADs), 1×10^6 cells were plated in 60 mm dishes for 24 hours followed by transfection with ^{m6}A-Tracer GFP (AddGene, 139403) and DAM-lamin B1 (AddGene, 119764) using Lipofectamine 3000 reagent (Thermo Fisher, L3000015) following the manufacturer's protocol. Briefly, 250 µl Opti-MEM medium (Thermo Fisher, 31985062) was mixed with 7.5 µl Lipofectamine 3000 reagent and incubated at 37 °C for 5 minutes. At the same time, 5 µg plasmid DNA was diluted in 250 µl Opti-MEM medium and incubated at 37 °C for 15 minutes. These two solutions were mixed and the DNA-lipid complexes were added to 1.5 ml DMEM medium without FBS and penicillin/streptomycin and incubated with cells at 37 °C for 12 hours. The media were then replaced with DMEM medium with 10% FBS and 1% penicillin/streptomycin. One day after transfection, ^{m6}A-Tracer GFP-labelled fibroblasts were seeded onto elastic and viscoelastic hydrogels and gels were fixed and immunostained for lamin B1 after 48 h of culturing for further imaging and analysis. To compare the continuity of the LAD between cells on elastic and viscoelastic matrices, the ratio of the fluorescence intensity of GFP to the fluorescence intensity of lamin B1 at the rim was calculated using an ImageJ macro. Briefly, individual nuclei were identified using Gaussian blur, thresholding, and analyze particle functions based on the fluorescence images of GFP expression or lamin B1 staining. The rim was segmented by subtracting the inner part from the whole nucleus and the average fluorescence intensity was measured.

Fluorescence recovery after photobleaching (FRAP)

Fibroblasts were seeded on hydrogels for 24 h and stained with Hoechst 33342 (Invitrogen) for FRAP experiments using a Leica TCS SP8 digital light sheet microscope with a pinhole of 2.5 to capture more spatial information. Briefly, a prescan of 6 images was acquired with an interval of 740 ms, followed by a bleaching pulse of 20 iterations at the selected area of 1 µm in diameter. 180 images were then taken with an interval of 1 s to record the changing fluorescence over time. For H2B-GFP fibroblasts expressing histone H2B with enhanced green fluorescent protein (EGFP), a prescan of 6 images was acquired with an interval of 740 ms, followed by a bleaching pulse of 2 iterations at the selected area of 2 µm in diameter. 80 images were then taken with an interval of 30 s to record the changing fluorescence over time. Analysis of FRAP movies were performed using a Jython script in ImageJ.

Chromatin-modifying enzyme activity assays

Nuclear protein extractions were isolated from 500,000 fibroblasts seeded on elastic and viscoelastic matrices for 48 h using a nuclear extraction kit (EpiGentek, OP-0002) according to the manufacturer's instructions. HAT, HDAC, H3K4 HMT, and H3K4 HDM activity were measured using the HAT activity/inhibition assay (EpiGentek, P-4003-048), HDAC activity/inhibition assay (EpiGentek, P-4034-096), HMT (H3K4 specific) activity/inhibition assay (EpiGentek, P-3002-1), and HDM (H3K4 specific) activity/inhibition assay (EpiGentek, P-3074-48), respectively. Per the manufacturer's instructions, 20 µg of nuclear extract was added into the assay wells and incubated at 37 °C for 90-120 min. After adding the color developer solution, the

absorbance was measured using a plate reader (Infinite 200Pro) at 450 nm for all the assays with the exception of the HDM (H3K4 specific) activity/inhibition assay where the fluorescence was measured at 530 EX/590 EM nm.

Assay for transposase-accessible chromatin using sequencing (ATAC-seq)

Sample collection, preprocessing and sequencing. 1,000,000 fibroblasts seeded on elastic or viscoelastic matrices were collected after 48 h and stored at -80 °C prior to sample processing, as previously described[36]. Frozen cells were thawed and washed once with PBS and then resuspended in 500 µL of cold PBS. The cell number was assessed by Cellometer Auto 2000 (Nexcelom Bioscience, Massachusetts, USA). 100,000 cells were then added to ATAC lysis buffer and centrifuged at 500 × g in a pre-chilled centrifuge for 5 min. Supernatant was removed and the nuclei were resuspended in 50 µL of tagmentation reaction mix by pipetting up and down. The reactions were incubated at 37 °C for 30 min in a thermomixer with shaking at 1000 rpm, and then cleaned up using the MiniElute reaction clean up kit (Qiagen). Tagmented DNA was amplified with barcoded primers. Library quality and quantity were assessed with Qubit 2.0 DNA HS Assay (Thermo Fisher), Tapestation High Sensitivity D1000 Assay (Agilent Technologies), and QuantStudio 5 System (Applied Biosystems). Equimolar pooling of libraries was performed based on QC values and sequenced on an Illumina NovaSeq (Illumina, California, USA) with a read length configuration of 150 PE for [100]M PE reads (50 m in each direction) per sample.

Data preprocessing, mapping, peak calling and downstream analysis. FASTQ files were trimmed with Trim Galore and cutadapt[42] after quality control checking. Pair-ended reads were then aligned to mouse reference genome (mm10) with Bowtie2[43]. Mitochondrial reads and PCR duplicates were removed using SAMtools[44] and Picard (http://broadinstitute.github.io/picard/) respectively. Peaks were called using MACS3[45] ($q < 0.001$), and only peaks outside the ENCODE blacklist regions were kept. All peaks from all samples were combined and merged using bedtools. FeatureCount[46] was used to count the mapped reads for each sample. Peaks that were up- or downregulated in different conditions were defined using DESeq2[47] with $P_{adj} = 0.05$ as the threshold and annotated using nearest genes and genomic features. Gene ontology (GO) enrichment analysis was then performed toward genes related to up- and down-regulated peaks using the enrichGO function in clusterProfiler package[48]. Peaks located at *cis*-regulatory elements related to genes of interest (± 5 kb region) were visualized using Integrative Genomics Viewer (IGV)[49] to demonstrate up- or down-regulated differential peaks. To compare the ATAC signals in Ascl1-, MyoD-, ETV2-, and Oct4-target binding sites across the genome in elastic and viscoelastic group, publicly available datasets (GSE43916, GSE157339, GSE168521, and GSE85602) were used to obtain the shared regions between the recognized peaks in these datasets and the differentially expressed ATAC peaks.

Lentiviral production and cell transduction

Dox-inducible lentiviral vectors for Tet-O-FUW-Ascl1, Tet-O-FUW-Brn2, Tet-O-FUW-Myt1l, Tet-O-FUW-GFP, and FUW-rtTA plasmids were used to transduce fibroblasts for ectopic expression of Ascl1, Brn2, Myt1l, GFP, and reverse tetracycline transactivator (rtTA). The STEMCCA lentiviral vector was used for the ectopic expression of OSKM[15]. Lentivirus was produced using established calcium phosphate transfection methods. Viral particles were collected and concentrated using Lenti-X Concentrator (Clontech) according to the manufacturer's protocol. Stable virus was aliquoted and stored at -80 °C. For viral transduction, fibroblasts were seeded and

allowed to attach overnight before incubation with the virus and polybrene (8 μg ml^{-1}, Sigma) for 24 h. After incubation, transduced cells were seeded onto hydrogels.

Direct reprogramming of fibroblasts into induced neuronal cells

Fibroblasts were transduced with lentivirus encoding BAM a day before being seeded onto hydrogels. After 24 h of cell seeding, the medium was changed to MEF medium containing doxycycline (Dox, 2 μg ml^{-1}, from Sigma) to activate transgene expression (day 0). On day 1, the medium was replaced with N3 medium: DMEM/F12 (Gibco) with the addition of N2 supplement (Invitrogen), B27 supplement (Invitrogen), 1% penicillin/streptomycin (Gibco), and Dox (2 μg ml^{-1}, from Sigma). Culture medium was replenished every other day during reprogramming to maintain the activity of the supplements. Cells were collected at day 2, 5, 7, 21, and 28 and analyzed to monitor the viscoelastic effects on cell phenotype conversion during the course of iN reprogramming.

Direct reprogramming of fibroblasts into induced pluripotent stem cells (iPSCs)

Fibroblasts were transduced with lentivirus encoding OSKM a day before being seeded onto hydrogels. Cells were kept in MEF medium for 48 h and then the medium was changed to mouse embryonic stem cell (mESC) medium: DMEM with the addition of 15% mouse ESC maintenance FBS (STEMCELL Technologies), 100 units ml^{-1} ESGRO mouse leukaemia inhibitory factor (mLIF, from Millipore), 0.1 mM β-mercaptoethanol (Sigma) and 1× MEM non-essential amino acid (Gibco). The medium was replenished every day for 10 days.

Quantitative reverse transcriptase-polymerase chain reaction

RNA was isolated from samples using Trizol (Ambion) according to the manufacturer's instructions. For cDNA synthesis, 500 ng of RNA was reverse transcribed using Maxima First Strand cDNA Synthesis Kit (Thermo Fisher Scientific). Template DNA was amplified using Maxima SYBR Green/Fluorescein qPCR Master Mix (Thermo Fisher Scientific) on a CFX qPCR machine (Bio-Rad). qRT-PCR data were analyzed using CFX Manager 3.1 (Bio-Rad) and gene expression levels (endogenous *Ascl1*: forward primer, CAACCGGGTCAAGTTGGTCA; reverse primer, CTCATCTTCTTGTTGGCCGC; *Tubb3*: forward primer, GCCGCTAGAGGTGAAATTC TTG; reverse primer, CATTCTTGGCAAATGCTTTCG) were normalized to the expression level of *18S* (forward primer, GCCGCTAGAGGTGAAATTCTTG; reverse primer, CATTCTTGGCAA ATGCTTTCG).

Chemical inhibition of histone deacetylase (HDAC)

To elucidate the role of HDAC in viscoelasticity-mediated iN reprogramming, cells cultured on tissue culture treated (TC) plates or gels for one day were treated with valproic acid (Cayman Chemical, 2.5 mg ml^{-1}) for 24 h. To examine the inhibition effects, after 24 h, cells on TC plates were collected for Western blotting analysis of AcH3 level. For reprogramming experiments, after 24 h treatment with valproic acid, medium was changed to MEF medium with Dox (2 μg ml^{-1}, from Sigma) to induce transgene expression (marked as day 0). After 24 h, the medium was changed to N3 medium and cells were cultured until day 7 to be fixed and immunostained for Tubb3.

Western blotting analysis

Alginate lyase (Sigma) was dissolved in PBS to make a 15 U ml^{-1} solution. The lyase solution was cooled down and added to the gels after washing gels with cold PBS once to dissolve the gels and collect the cells. Cells were then lysed in RIPA buffer (Thermo Scientific, 89900) along with protease & phosphatase inhibitor cocktail (Thermo Scientific, 78440) on ice. Protein lysates were centrifuged to pellet cell debris, and the supernatant was collected and used for further analysis. Protein samples were run using SDS-PAGE and transferred to polyvinylidene fluoride membranes. Membranes were blocked in 5% nonfat milk and incubated with primary antibodies (**Table S1, Supplementary Information**) overnight on ice. Membranes were washed with Tris-Buffered Saline + 0.05% Tween-20 and incubated with HRP-conjugated IgG secondary antibodies (Santa Cruz Biotechnologies) for 1 h. Protein bands were visualized using Western Lightning Plus-Enhanced Chemiluminscence Substrate (Perkin Elmer Life & Analytical Sciences) and imaged on a ChemiDoc XRS system (Bio-Rad).

Statistical analysis

The data were presented as mean plus or minus one standard deviation, where $n \geqslant 3$. The data corresponding to the cell spreading area, nuclear volume, chromatin compaction index, and histone quantification experiments were displayed as truncated violin plots to demonstrate the distribution of data. The violins were drawn with the ends at the quartiles and the median as a horizontal line in the violin. Comparisons among values for groups greater than two were performed using a one-way or two-way analysis of variance (ANOVA) and differences between groups were determined using the following multiple comparison tests: Dunnett's, Tukey's, and Sidak's post-hoc test. For comparison between two groups, a two-tailed, unpaired t-test was used. For all cases, p-values less than 0.05 were considered statistically significant. GraphPad Prism 9.0 were used for all statistical analysis.

References

42 Martin, M. Cutadapt removes adapter sequences from high-throughput sequencing reads. *EMBnet.journal* **17**, doi:10.14806/ej.17.1.200 (2011).

43 Langmead, B. & Salzberg, S. L. Fast gapped-read alignment with Bowtie 2. *Nat. Methods* **9**, 357-359, doi:10.1038/nmeth.1923 (2012).

44 Danecek, P. *et al.* Twelve years of SAMtools and BCFtools. *Gigascience* **10**, doi:10.1093/gigascience/giab008 (2021).

45 Zhang, Y. *et al.* Model-based analysis of ChIP-Seq (MACS). *Genome Biol.* **9**, R137, doi:10.1186/gb-2008-9-9-r137 (2008).

46 Liao, Y., Smyth, G. K. & Shi, W. featureCounts: an efficient general purpose program for assigning sequence reads to genomic features. *Bioinformatics* **30**, 923-930, doi:10.1093/bioinformatics/btt656 (2014).

47 Love, M. I., Huber, W. & Anders, S. Moderated estimation of fold change and dispersion for RNA-seq data with DESeq2. *Genome Biol.* **15**, 550, doi:10.1186/s13059-014-0550-8 (2014).

48 Wu, T. *et al.* clusterProfiler 4.0: A universal enrichment tool for interpreting omics data. *Innovation (Camb)* **2**, 100141, doi:10.1016/j.xinn.2021.100141 (2021).

49 Robinson, J. T. *et al.* Integrative genomics viewer. *Nat. Biotechnol.* **29**, 24-26, doi:10.1038/nbt.1754 (2011).

Data Availability

Sequencing data will be available at the GEO after publication. Previously published data that were used in this paper are available at the GEO under accession codes GSE43916, GSE157339, GSE168521, and GSE85602. Source data are provided with this paper. All other data supporting the findings of this study are available from the corresponding authors upon reasonable request.

Code availability

Codes utilized for image analysis and sequencing data analysis are available on the lab website (https://li-lab.seas.ucla.edu/requestform/).

Acknowledgements

This work was supported, in part, by a UCLA Eli and Edythe Broad Center of Regenerative Medicine and Stem cell Research Innovation Award; grants from the National Institute of Health (GM143485 and NS130677 to S.L.); a fellowship from the National Science Foundation GRFP (to J.S.); a postdoctoral fellowship from the National Institute of Arthritis and Musculoskeletal and Skin Diseases of the NIH under the Ruth L. Kirschstein National Research Service Award (T32AR059033, to J.S.). The authors acknowledge the support by the NIH/NCI under award number P30CA016042 and the Advanced light Microscopy and Spectroscopy Laboratory at the California NanoSystems Institute. The content is solely the responsibility of the authors and does not necessarily represent the official views of the NIH.

Author Contributions

Y.W. and S.L. conceived the study. Y.W., Y.S., and S.L. designed the experiments. Y.W., Y.S., J.S., T.H., A.Z., and X.H. performed the experiments. Y.W., Y.S., J.S., and T.H analyzed the data. Z.F., J.E. and L.G. provided the reagents. Y.W., Y.S., J.S., T.H., Z.F., J.E., L.G., Z.G., and S.L. contributed to the data interpretation and discussion. Y.W., J.S., and S.L. wrote the manuscript.

Competing Interests Statement

Y.W., Y.S., J.S., and S.L. have filed a patent application.

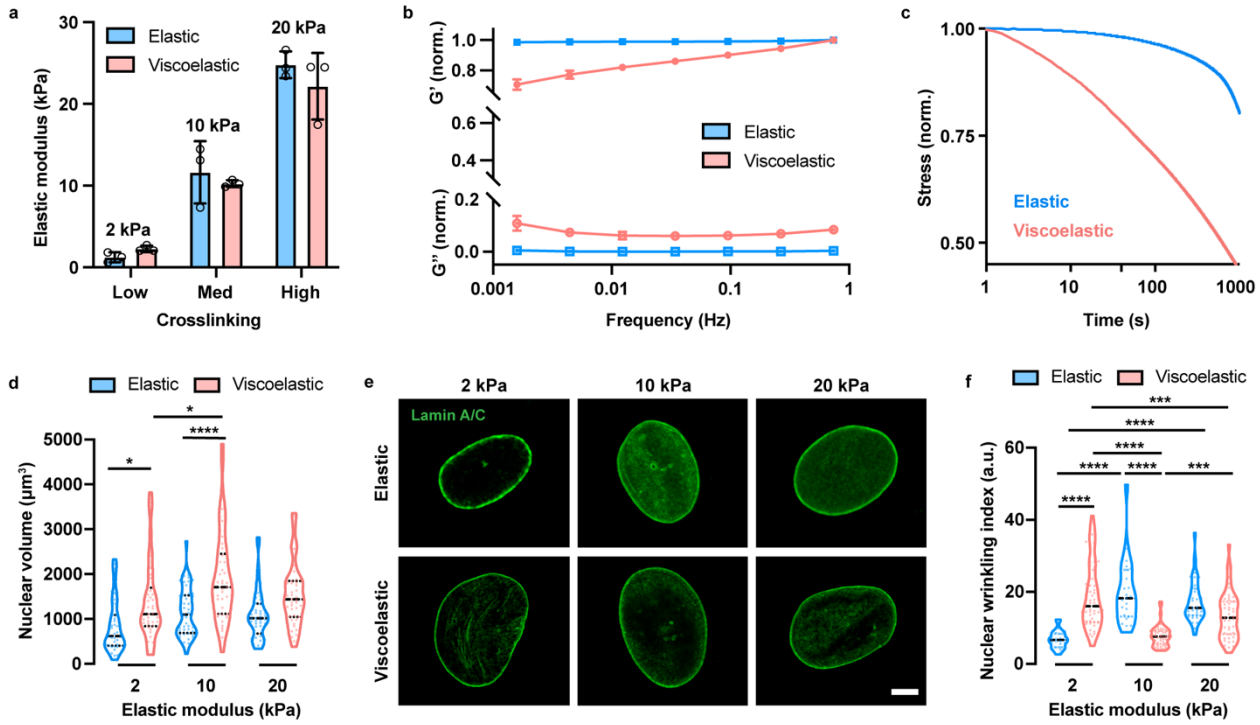

Figure 1. Viscoelastic matrices increase nuclear volume and alter the nuclear lamina in a stiffness-dependent manner. a, Initial elastic modulus of covalently (elastic) or ionically (viscoelastic) crosslinked alginate hydrogels with different concentrations of crosslinkers measured by compression tests (n = 3 gels). **b**, Storage modulus (G') and loss modulus (G'') of alginate gels at varying frequencies (n = 3 gels). Values are normalized by the storage modulus at 1 rad s^{-1} of the gels presented. **c**, Stress relaxation of elastic and viscoelastic gels as a function of time under a constant deformation. **d**, Nuclear volume of primary mouse fibroblasts cultured on elastic and viscoelastic matrices for 24 hours (n = 39, 38, 47, 43, 40, 43 cells from 3 gels per condition). **e**, Immunofluorescence images of lamin A/C staining of cells cultured on different surfaces for 2 days. Scale bar, 5 μm. **f**, Quantification of nuclear wrinkling based on the inner fluorescence intensity of the staining (n = 27, 48, 23, 52, 35, 51 cells from 3 gels per condition). In **a**, **b**, and **g**, data are shown as mean $\pm$ s.d. In **d** and **f**, truncated violin plots were used to demonstrate the distribution of data. The violins are drawn with the ends at the quartiles and the median as a horizontal line in the violin, where the curve of the violin extends to the minimum and maximum values in the data set. Significance was determined by one-way ANOVA using Tukey's correction for multiple comparisons (*$P < 0.05$, ***$P < 0.001$, ****$P < 0.0001$).

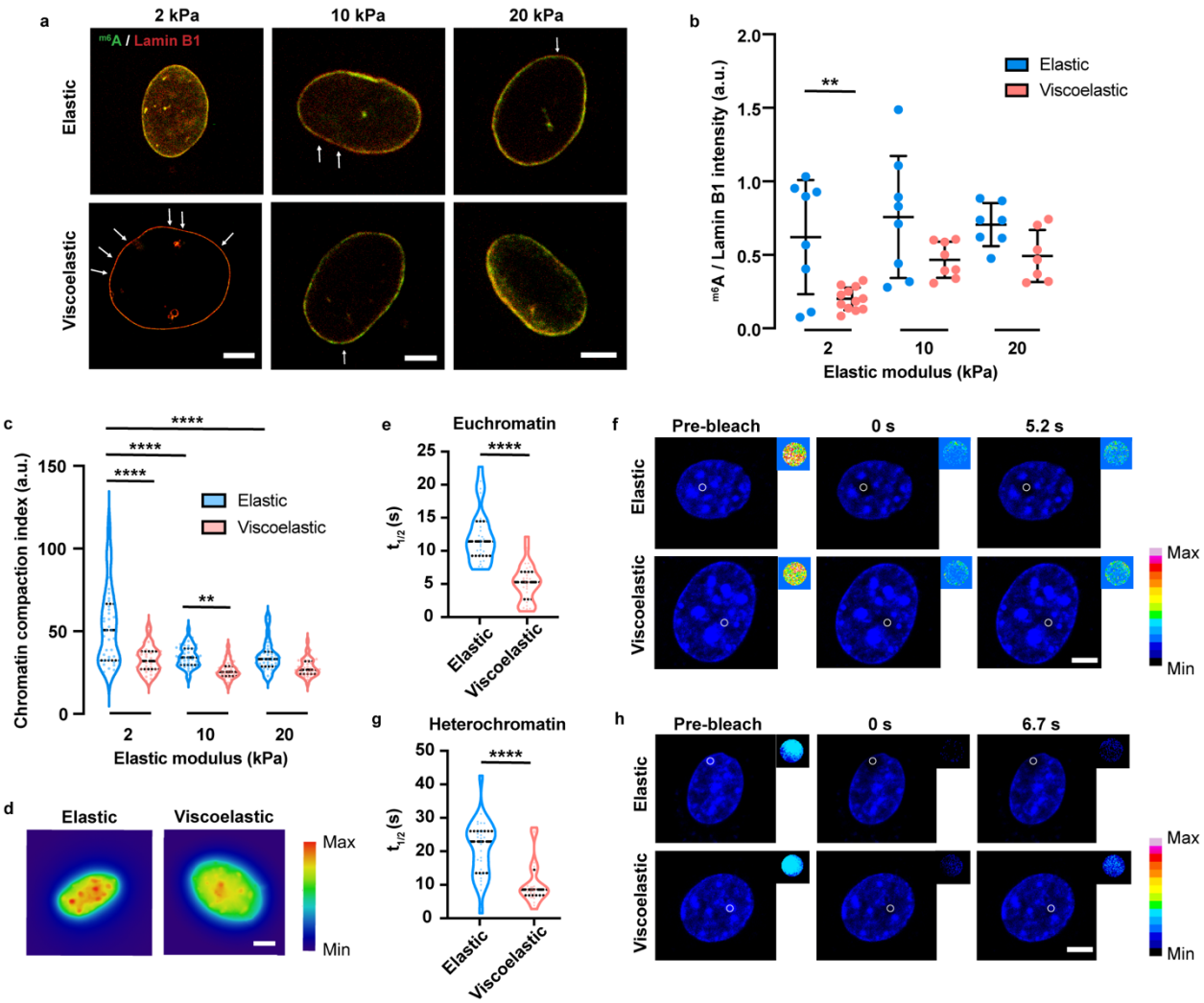

Figure 2. Viscoelastic matrices disrupt lamina associated domains (LADs), decrease chromatin condensation, and enhance chromatin dynamics. a, Confocal images of ^{m6}A-tracer-labeled LADs in the cell nucleus on different gels, where cells were cultured on various matrices for 2 days and immunostained for lamin B1 to characterize the co-location of LADs and the nuclear lamina. White arrows indicate regions where there is detachment loci of LADs. Scale bar, 10 μm. **b**, Quantification of the fluorescence intensity of ^{m6}A-tracer at the rim normalized by the fluorescence intensity of lamin B1 staining to indicate the spatial distribution of LADs (n = 8, 12, 9, 8, 8, 8 cells). **c**, Chromatin compaction index of fibroblasts plated on elastic and viscoelastic matrices for 24 hours, quantified by using the ratio of the integrated fluorescence intensity of DAPI staining to nuclear volume (n = 39, 38, 47, 43, 40, 43 cells from 3 gels per condition). **d**, Representative images of a DAPI-stained cell nucleus on elastic or viscoelastic surfaces. Scale bar, 5 μm. **e-f**, Truncated violin plots showing the recovery half time ($t_{1/2}$, the time taken for the bleached region to reach half of its final intensity) of photo-bleached areas (white circle) in euchromatic regions (**e**) and the representative images demonstrating the fluorescence recovery after photo-bleaching in cells cultured on elastic or viscoelastic matrices for 24 hours (**f**). Squares on the top right corner of each images indicate the fluorescence intensity in the photo-bleached

area. **g-h**, Truncated violin plots showing the recovery half time of bleached areas (white circle) in heterochromatic regions (**g**) and the representative images demonstrating the fluorescence recovery after photo-bleaching in cells cultured on elastic or viscoelastic matrices for 24 hours (**h**). Squares on the top right corner of each image indicates the fluorescence intensity in the photo-bleached area. In **b**, data are shown as mean $\pm$ s.d. In **c**, **e**, and **g**, the violins are drawn with the ends at the quartiles and the median as a horizontal line in the violin, where the curve of the violin extends to the minimum and maximum values in the data set. In **b** and **c**, significance was determined by one-way ANOVA using Tukey's correction for multiple comparisons (**$P < 0.01$, ****$P < 0.0001$). In **e** and **g**, a two-tailed, unpaired t test was used to determine the statistical significance (****$P < 0.0001$).

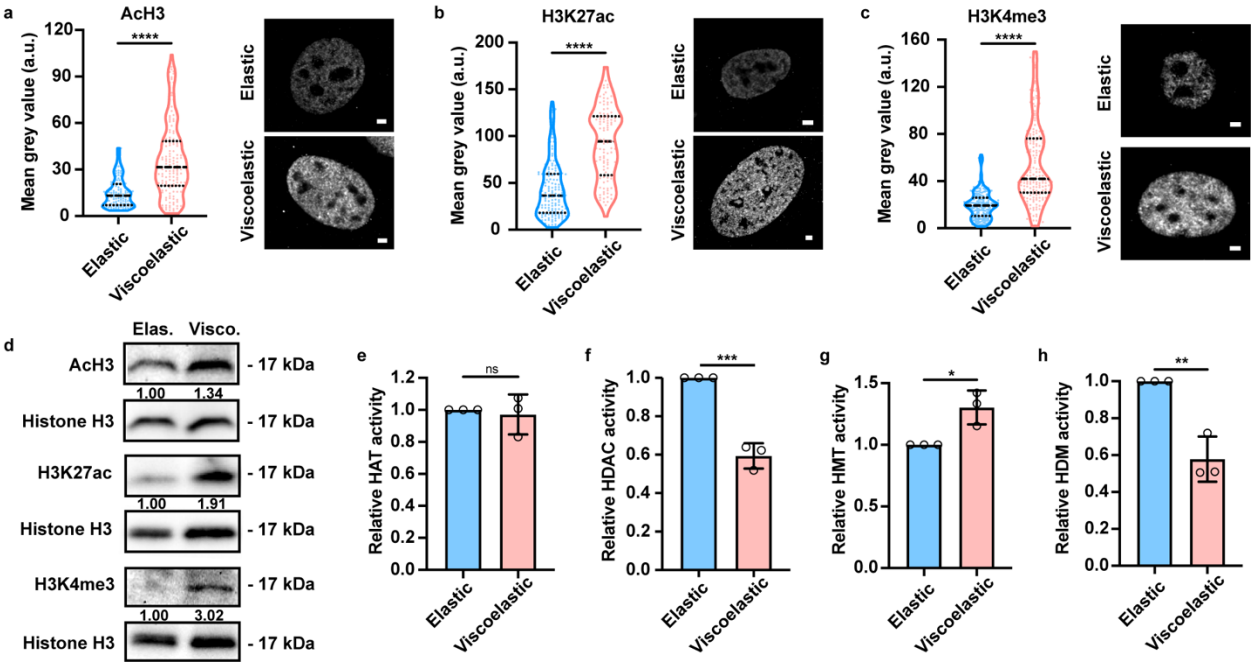

Figure 3. Viscoelastic matrices facilitate open chromatin structure. a-c, Truncated violin plots showing the fluorescence intensity quantification (left) for histone H3 acetylation (AcH3, **a**), histone H3 lysine 27 acetylation (H3K27ac, **b**), and tri-methylated histone H3 on lysine 4 (H3K4me3, **c**) in mouse fibroblasts cultured on elastic or viscoelastic matrices of 2 kPa for 48 hours (n = 111, 142 cells from 3 gels per condition for AcH3; 154, 104 cells from 3 gels per condition for H3K27ac; 215, 180 cells from 3 gels per condition for H3K4me3). Representative images on the right show the corresponding histone modifications. Scale bar, 2 μm. **d**, Western blotting analysis of AcH3 (top), H3K27ac (middle), and H3K4me3 (bottom). The values indicate the protein expression level normalized to the corresponding histone H3 and elastic groups. **e-f**, Quantification of histone acetyltransferase (HAT) activity (**e**) and histone deacetylase (HDAC) activity (**f**) in cells cultured on elastic or viscoelastic matrices for 48 hours (n = 3 gels). **g-h**, Quantification of H3K4-specific histone methyltransferase (HMT) activity (**g**) and histone demethylase (HDM) activity (**h**) in cells cultured on elastic or viscoelastic matrices for 48 hours (n = 3 gels). For truncated violin plots in **a-c**, the violins are drawn with the ends at the quartiles and the median as a horizontal line in the violin, where the curve of the violin extends to the minimum and maximum values in the data set. In **e-h**, bar graphs show the mean $\pm$ s.d. In **a-c** and **e-h**, a two-tailed, unpaired t test was used to determine the statistical significance (*$P < 0.05$, **$P < 0.01$, ***$P < 0.001$, ****$P < 0.0001$).

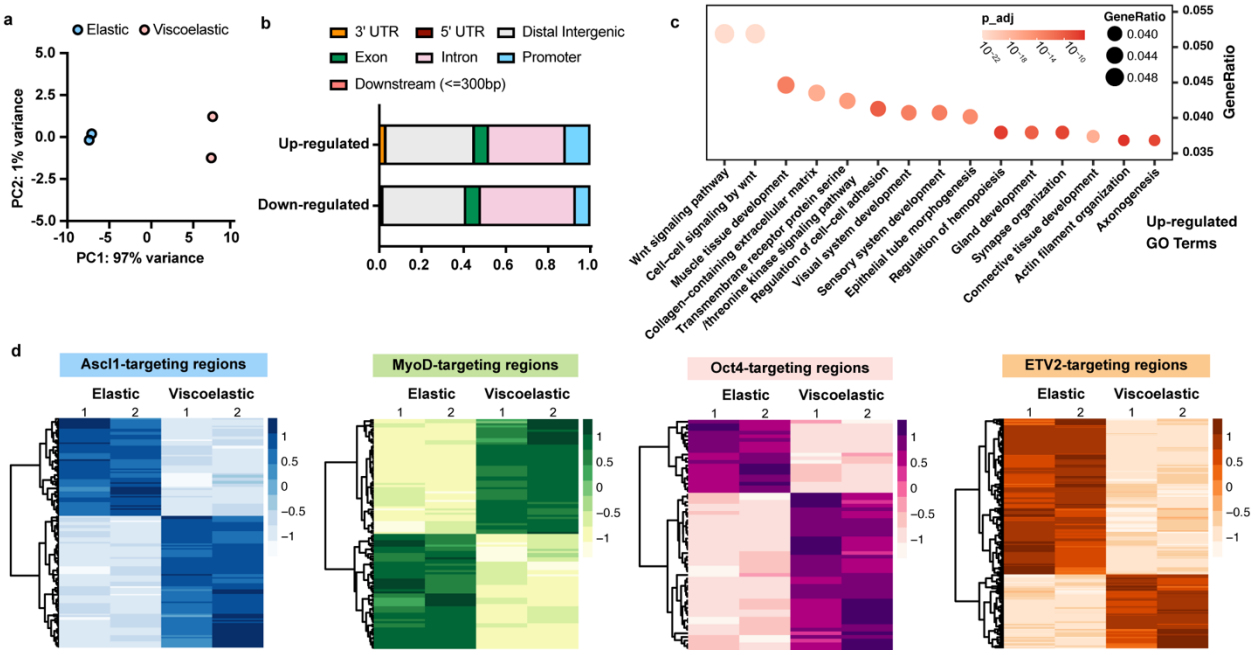

Figure 4. Viscoelastic matrices regulate genome-wide chromatin accessibility. a, Principal component analysis (PCA) of ATAC-seq data from independent biological replicates of mouse fibroblasts cultured on elastic or viscoelastic matrices for 48 hours (n = 2 gels). **b**, Percentage of genomic features associated with up- or down-regulated ATAC peaks in viscoelastic groups in comparison with elastic groups. **c**, Top 15 gene ontology (GO) enriched terms in up-regulated peaks of viscoelastic groups. **d**, Heatmaps showing the signals in the overlapping regions between Ascl1-, MyoD-, Oct4-, or ETV2-targeting binding sites and differentially expressed ATAC peaks, respectively (left to right).

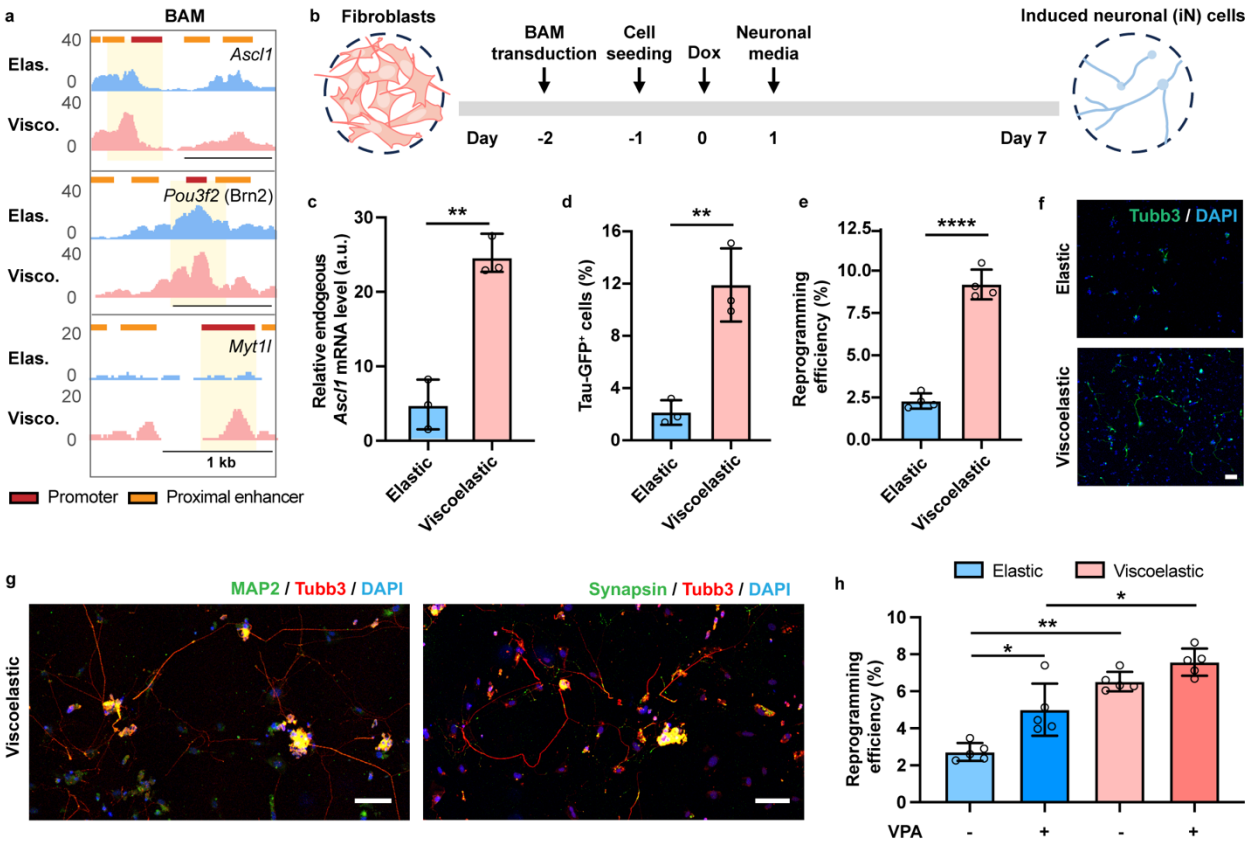

Figure 5. Matrix viscoelasticity enhances the reprogramming of fibroblasts into induced neuronal (iN) cells. a, ATAC peaks around the promoters of *Ascl1*, *Pou3f2* (Brn2), and *Myt1l* in fibroblasts cultured on elastic and viscoelastic matrices. **b**, Schematic illustration of the reprogramming timeline. **c**, Endogenous *Ascl1* mRNA expression in BAM-transduced cells on elastic or viscoelastic matrices on day 2 after doxycycline (Dox)-induced transgene expression (n = 3). **d**, Percentage of cells expressing Tau-GFP on different matrices at day 5 (n = 3). **e**, Reprogramming efficiency of BAM-transduced fibroblasts cultured on elastic or viscoelastic matrices at day 7, which was determined from the percentage of Tubb3$^+$ cells among the total number of cells initially seeded on different gels (n = 4). **f**, Representative fluorescent images showing Tubb3$^+$ cells at day 7 on different matrices. Scale bar, 100 μm. **g**, Representative fluorescent images showing Tubb3$^+$ iN cells co-expressing mature neuronal markers, MAP2 at day 21 or synapsin at day 28, on viscoelastic surfaces. Scale bar, 100 μm. **h**, Quantification of the reprogramming efficiency of fibroblasts cultured on various surfaces in the absence or presence of an HDAC inhibitor (valproic acid, VPA) (n = 5). In **c-e** and **h**, bar graphs show the mean $\pm$ s.d. In **c-e**, a two-tailed, unpaired t test was used to determine statistical significance, whereas in **h**, a two-way ANOVA using Tukey's correction for multiple comparisons was used to determine the significance between the groups (*$P < 0.05$, **$P < 0.01$, ****$P < 0.0001$).

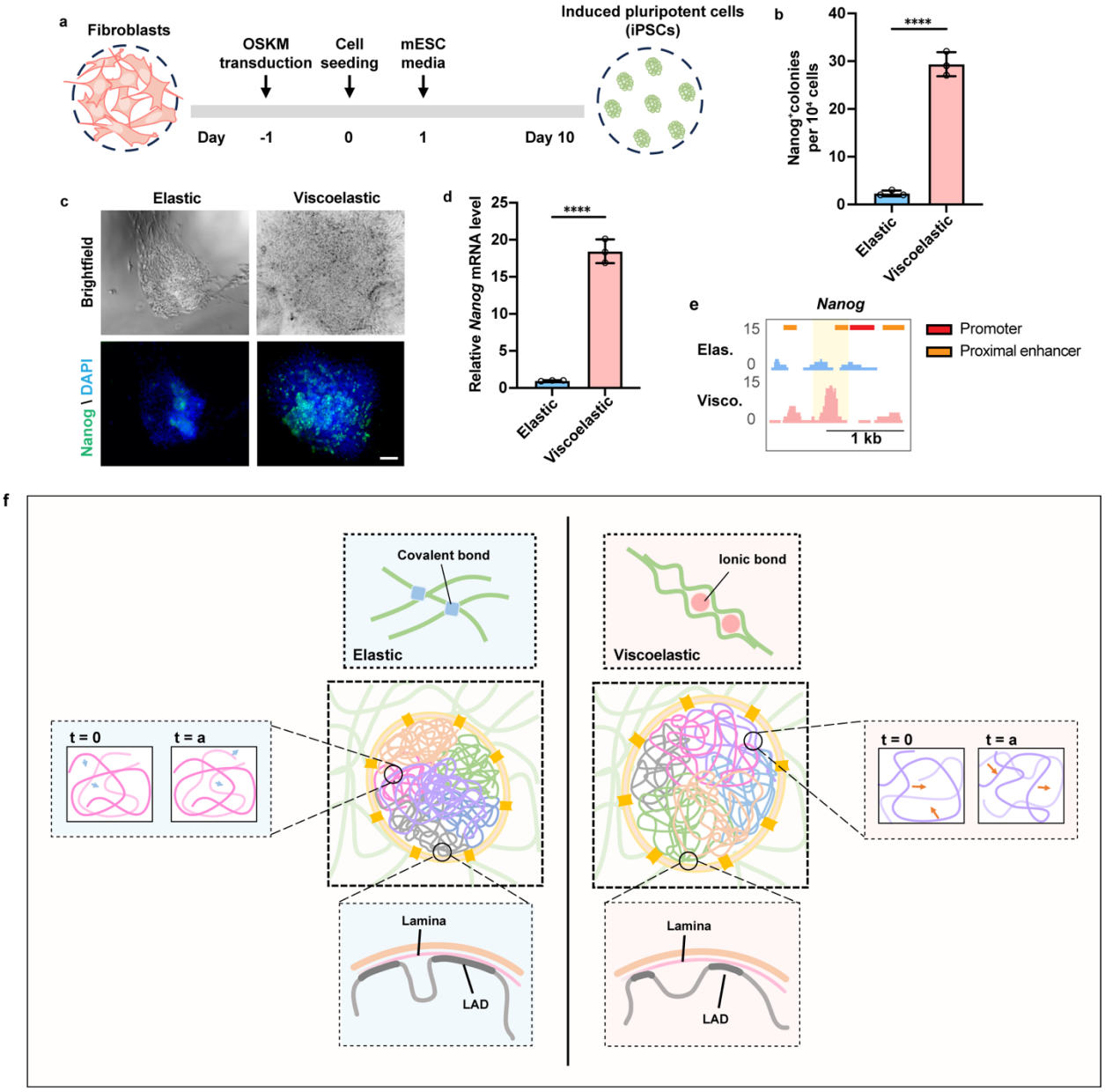

Figure 6. Matrix viscoelasticity promotes the reprogramming of fibroblasts into induced pluripotent stem cells (iPSCs). a, Schematic illustration of the reprogramming timeline. **b**, Quantification of Nanog$^+$ colonies on elastic or viscoelastic matrices at day 10 (n = 3). **c**, Representative brightfield (top) and fluorescent (bottom) images of Nanog$^+$ colonies on elastic or viscoelastic matrices at day 10. Scale bar, 100 μm. **d**, PCR analysis of *Nanog* mRNA expression in cells on various surfaces at day 10 (n = 3). **e**, ATAC peaks around the promoter region of *Nanog* in elastic and viscoelastic groups. **f**, Schematic summary of the viscoelastic effects on cell nucleus, chromatin, and the epigenome on soft matrices. Our findings demonstrate that cells on viscoelastic matrices have larger cell nucleus, loosely organized chromatin, faster chromatin dynamics, and more open chromatin structure, in comparison with elastic matrices, which suggests the potential viscoelastic effects on cellular plasticity that encourages cell phenotype transitions on viscoelastic

matrices. In **b** and **d**, bar graphs show the mean ± s.d. and a two-tailed, unpaired t test was used to determine statistical significance (****$P < 0.0001$).